Research Square

Preprints are preliminary reports that have not undergone peer review.
They should not be considered conclusive, used to inform clinical practice,
or referenced by the media as validated information.

Chemical Disorder Suppresses Thermal Transport through Local Stress Redistribution in SrTiO3-Based High-Entropy Perovskites

Yongheng Li
Zhongguancun Institute of Artificial Intelligence
Maomao Liu
Henan Polytechnic University
Hongwei Du
Zhongguancun Institute of Artificial Intelligence
Baole Wei
Zhongguancun Institute of Artificial Intelligence
Bin Wei
Henan Polytechnic University
Bonan Zhu
bzhu@bit.edu.cn
Beijing Institute of Technology
Ziheng Lu
Zhongguancun Institute of Artificial Intelligence
Yuanhua Lin
Tsinghua University

Article

Keywords:

Posted Date: September 7th, 2026

DOI: https://doi.org/10.21203/rs.3.rs-10754513/v1

License: This work is licensed under a Creative Commons Attribution 4.0 International License.
Read Full License

Additional Declarations: No competing interests reported.

Chemical Disorder Suppresses Thermal Transport through Local Stress Redistribution in $SrTiO_3$-Based High-Entropy Perovskites

Yongheng Li[1], Maomao Liu[2], Hongwei Du[1], Baole Wei[1], Bin Wei[2,*], Bonan Zhu[1,3,*], Ziheng Lu[1,*], Yuanhua Lin[4]

[1]Zhongguancun Institute of Artificial Intelligence, Beijing 100094, China
[2]Henan Key Laboratory of Materials on Deep-Earth Engineering, School of Materials Science and Engineering, Henan Polytechnic University, Jiaozuo 454000, China
[3]School of Aerospace Engineering, Beijing Institute of Technology, Beijing 100081, China
[4]State Key Laboratory of New Ceramics and Fine Processing, School of Materials Science and Engineering, Tsinghua University, Beijing 100084, China
*Corresponding: binwei@hpu.edu.cn, bzhu@bit.edu.cn, luziheng@zgci.ac.cn

Abstract

High-entropy disorder offers an effective route to suppress lattice heat transport in oxide thermoelectrics, yet the atomistic origin of phonon scattering in high-entropy $SrTiO_3$ remains unresolved. Here, we distill a fine-tuned MACE teacher into an accurate and efficient NEP for large-scale molecular dynamics. Using this potential, we find that A-site substitution rapidly lowers lattice thermal conductivity, while further reductions are modest in the four- and five-component compositions near 3 W m^{-1} K^{-1}. Phonon spectra reveal two distinct dopant effects: Pb introduces a low-frequency soft-mode-like response, whereas Ca produces stronger spectral broadening. Mass fluctuation and ionic-size mismatch alone do not describe the conductivity trend well. Instead, the local stress descriptor correlates more directly with thermal conductivity and captures the loss of phonon spectral coherence, linking local stress disorder to effective lifetime-like broadening. These results establish local stress disorder as a transport descriptor for low thermal conductivity and show that MACE-guided NEP distillation provides a practical route to large-scale atomistic studies of high-entropy oxides.

Introduction

Suppressing lattice heat conduction while preserving useful carrier transport is a central challenge in thermoelectric materials. Oxide thermoelectrics are attractive because of their thermal stability, chemical robustness and tolerance to aliovalent doping, yet their relatively high lattice thermal conductivity remains a persistent limitation [1, 2]. $SrTiO_3$ (STO) is a representative perovskite oxide thermoelectric platform: its electronic transport can be tuned by A-site and B-site substitution, oxygen non-stoichiometry and carrier doping, while its corner-sharing octahedral framework provides a model lattice for studying phonon transport in chemically complex oxides. Entropy engineering has recently emerged as a powerful route for reducing lattice thermal conductivity in thermoelectrics [3]. In high-entropy chalcogenides and GeTe-based alloys, entropy stabilization and multi-component disorder have produced high thermoelectric performance by combining low lattice thermal conductivity with favorable electronic-structure effects [4, 5]. Related studies in half-Heusler, Ag-based chalcogenide and Bi_2Te_3-based systems further show that high-entropy or entropy-engineered disorder can introduce mass fluctuation, strain-field fluctuation, local structural distortion, phonon-spectrum reconstruction and mesoscale heterogeneity [6–9]. In oxides, entropy-stabilized and high-entropy perovskites show that chemical disorder can be translated into low thermal conductivity through many factors, such as strain fields and local lattice

distortion [2, 10, 11]. Recent experiments on high-entropy STO-based ceramics have reported A-site short-range disorder together with reduced thermal conductivity, and entropy engineering has also been used to promote carrier-phonon decoupling in perovskite thermoelectrics [2, 11]. For high-entropy STO, the key remaining question is therefore which component of the A-site disorder field is transmitted through the TiO_6 framework and most strongly suppresses heat transport.

The broader challenge is to move from entropy as a compositional label to disorder as a set of physically separable transport descriptors. Reviews and recent mechanism studies have made clear that low thermal conductivity in high-entropy thermoelectrics cannot be reduced to a single scattering channel: mass and strain fluctuations, local lattice distortion, phonon localization, spectrum broadening, chemical short-range order and atomic-to-nanoscale chemical fluctuations can all contribute, depending on the host lattice and the active sublattice [3, 6, 12–15]. The difficulty is that composition-level descriptors are not independent materials knobs. The same nominal configurational entropy can correspond to different distributions of mass contrast, ionic-size mismatch, local strain and octahedral distortion, and their effect on phonons is filtered through lattice connectivity, lattice stiffness and the relaxation of local distortions over multiple length scales. This descriptor entanglement is especially acute in perovskite oxides: A-site disorder is mechanically coupled to the corner-sharing TiO_6 network, so a nominal A-site perturbation can be transmitted into Ti-O distortions, local stress fields, etc. Average structural refinement and macroscopic thermal-transport measurements can establish that entropy engineering works, but they cannot by themselves determine which local descriptor controls the residual crystalline heat flow after strong disorder has been introduced. A descriptor-level understanding therefore requires atomistic access to how chemical disorder reshape phonon spectra and heat-carrying modes. High-entropy STO provides a representative oxide-perovskite platform for examining how composition-level A-site disorder is converted into relaxed local lattice responses and phonon-scattering descriptors.

Constructing potentials for high-entropy oxides is challenging, especially when the chemical space contains elements that exhibit relatively large machine-learning force-field fitting errors. Systematic elemental benchmarks have reported particularly large errors for early transition metals in the middle of the periodic table[16]. La-containing compounds have likewise motivated dedicated dataset construction, training and validation strategies in deep-potential and solid-state-electrolyte studies [17, 18]. In high entropy materials, random occupation of multiple A-site species, including La, creates complex local chemical environments, while phonon and thermal transport simulation in disordered structures require large supercells and long trajectories. Directly training an interatomic potential from scratch for this space would require a prohibitive number of density functional theory (DFT) labelled configurations, and a potential trained on insufficient data may reproduce energies while failing for forces, stresses or heat-transport properties.

Here, we use a two-step fine-tuned MACE-guided NEP distillation workflow to meet these requirements. A pretrained MACE model is first fine-tuned with DFT-labelled configurations spanning the Sr/Ba/Ca/Pb/La A-site chemical space of STO-based high-entropy oxides, which substantially improves both energy and force predictions relative to the pretrained model. The fine-tuned MACE model is then used as a teacher model to distill an efficient neuroevolution potential (NEP), retaining the fidelity required for thermal-transport simulations while enabling large-scale MD. Using the distilled NEP, we show that A-site disorder drives a rapid reduction of lattice thermal conductivity from crystalline STO, but the reduction becomes much slower in the four- and five-component compositions near 3 W m^{-1} K^{-1}, remaining above the Cahill-Pohl limit of approximately 1.84 W m^{-1} K^{-1}. We disentangle the effects of mass disorder, size mismatch and local von Mises stress on thermal transport. Ca-induced size disorder suppresses heat transport more strongly than Pb-induced mass disorder, producing greater spectral broadening and loss of coherent spectral weight. Neither mass fluctuation nor ionic-size mismatch alone captures the

conductivity trend. The local stress descriptor correlates more strongly with thermal conductivity and with the loss of phonon spectral coherence, linking stress disorder to effective lifetime-like broadening. These results show that MACE-guided NEP distillation as an effective route for studying thermal transport in high-entropy perovskite oxides, as well as establish stress disorder as a transport descriptor.

Results

We first compare the fine-tuned MACE, directly trained NEP and MACE-distilled NEP models for the high-entropy $A\mathrm{TiO_3}$ configuration space, where the A site is occupied by Sr, Ba, Pb, Ca and La. Before fine-tuning, the pretrained MACE model gives test-set mean absolute errors of 2.09 meV atom^{-1} for energy, 43.98 meV Å^{-1} for force and 6.38 meV Å^{-3} for stress. Fine-tuning on 615 DFT-labelled structures lowers these errors to 0.73 meV atom^{-1}, 31.85 meV Å^{-1} and 2.80 meV Å^{-3}, respectively. The training-set errors show a similar improvement. The energy and force errors decrease from 2.16 to 0.79 meV atom^{-1} and from 42.86 to 29.68 meV Å^{-1}, respectively (Fig. 1a,d). The stress error decreases from 6.26 to 2.74 meV Å^{-3} (Fig. S1).

Thermal-transport calculations of disordered structures require large supercells, long trajectories and repeated sampling of disordered configurations, so the potential must combine accuracy with low computational cost. When trained on 615 DFT-labelled structures from the La-containing target space, the direct NEP gives test-set mean absolute errors of 13.73 meV atom^{-1} for energy and 160.51 meV Å^{-1} for force. The corresponding training-set errors are 12.00 meV atom^{-1} and 157.98 meV Å^{-1}, respectively (Fig. 1b,e). Because fitting accuracy depends on both chemical elements and model architecture [16], we used Cd as a direct-fitting control for the La-containing system. We replaced La with Cd and trained a direct NEP using the same number of DFT-labelled structures. The Cd-containing model gives test-set mean absolute errors of 0.78 meV atom^{-1} for energy and 66.88 meV Å^{-1} for force (Fig. S2). These much lower errors show that the La-containing chemical space is considerably more difficult for direct NEP fitting, motivating the use of teacher-guided distillation.

Distillation reduces the NEP errors in La-containing systems. Against DFT, the distilled NEP gives test-set mean absolute errors of 2.81 meV atom^{-1} for energy and 57.78 meV Å^{-1} for force. The corresponding training-set errors are 2.77 meV atom^{-1} and 53.95 meV Å^{-1}, respectively (Fig. 1c,f). The distilled model is less accurate than the fine-tuned MACE teacher but much more accurate than the direct NEP, while retaining the computational efficiency required for large cells and long MD trajectories. We therefore use the distilled NEP for the thermal-transport and phonon-dynamics calculations. As a transport-level check, it predicts a lattice thermal conductivity of 8.93 W m^{-1} K^{-1} for pristine crystalline Pm$\bar{3}$m STO, consistent with the previously reported NEP range of approximately 8–9 W m^{-1} K^{-1} [19].

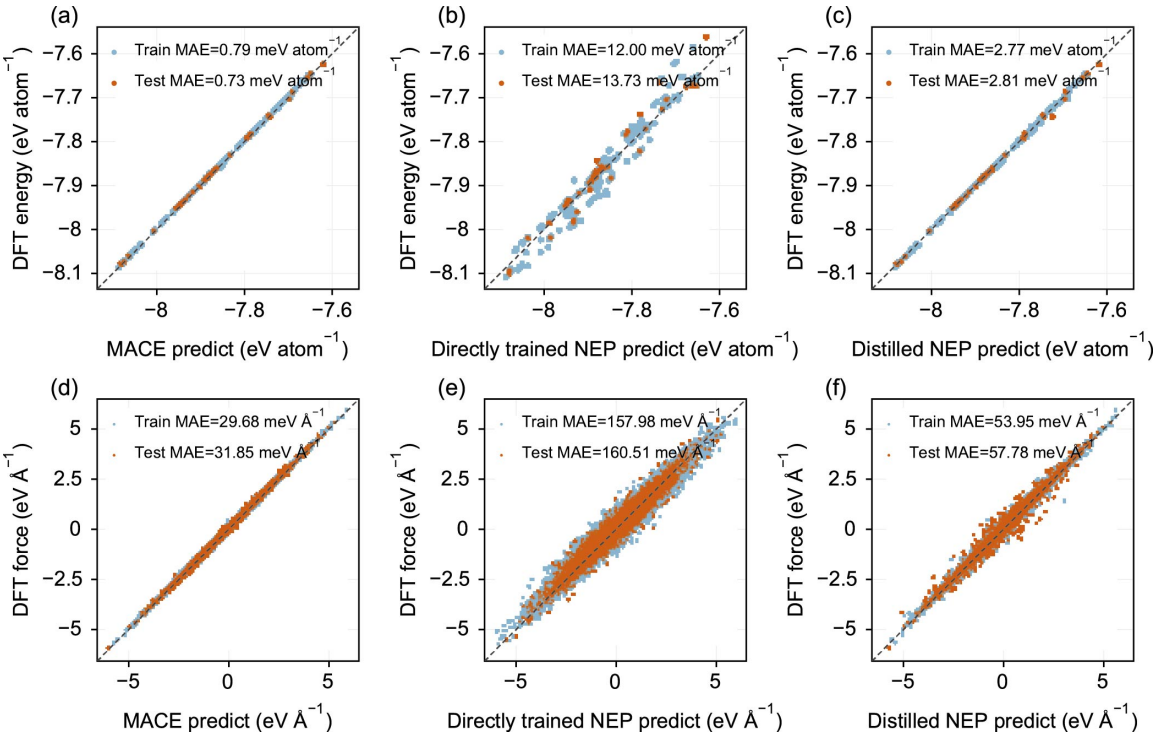


Figure 1: Validation of the MACE-guided NEP distillation workflow. (a,d) Energy and force predictions of the fine-tuned MACE teacher model compared with DFT reference data. (b,e) Energy and force predictions of a NEP model trained directly on the DFT-labelled structures. (c,f) Energy and force predictions of the MACE-distilled NEP model compared with DFT.

We next examine the relaxed structures of the A-site-substituted STO systems. The representative compositions in Fig. 2a, $SrTiO_3$, $Sr_{0.8}Pb_{0.2}TiO_3$, $Sr_{0.8}Ca_{0.2}TiO_3$, $Sr_{0.4}Ca_{0.4}La_{0.2}TiO_3$ and $Sr_{0.2}Ba_{0.2}Ca_{0.2}Pb_{0.2}La_{0.2}TiO_3$, all retain the perovskite framework. A-site substitution nevertheless produces increasingly heterogeneous local environments around the TiO_6 network. The total radial distribution functions (RDFs) in Fig. 2b quantify these structural changes. The nearest Ti-O peak remains near 1.98 Å, whereas the largest composition-dependent differences occur between 4 and 5 Å. Analysis of the element-resolved pair correlations shows that the feature near 4.3–4.4 Å arises mainly from higher-order Ti-O correlations, whereas the feature near 4.7–4.8 Å contains mixed A-O and O-O contributions. Pb and Ca substitution produce distinct structural responses associated with mass and size disorder, respectively. Although Pb produces a much larger A-site mass fluctuation, $Sr_{0.8}Pb_{0.2}TiO_3$ retains sharper RDF features between 4 and 5 Å than $Sr_{0.8}Ca_{0.2}TiO_3$. The Ca-containing system shows stronger broadening and weakening of these features despite its smaller mass fluctuation, consistent with greater distortion from ionic-size mismatch. As additional A-site species are introduced, the second feature in this region broadens further. This trend shows that multicomponent A-site disorder extends beyond nearest-neighbor bonds and modifies medium-range structural correlations.

To distinguish the mass and size components of A-site compositional disorder, Figs. 2c and 2d compare two descriptors calculated from the elemental fractions of each composition. Following the mass-fluctuation treatment used in multicomponent thermoelectric transport studies [20], the A-site mass descriptor is defined relative to the composition-weighted average atomic mass,

$$M_{\mathrm{avg}} = \sum_i x_i M_i, \qquad \delta_{\mathrm{mass}} = \sum_i x_i \left(1 - \frac{M_i}{M_{\mathrm{avg}}}\right)^2, \tag{1}$$

where x_i and M_i are the A-site molar fraction and standard atomic mass of element i, respectively. Ionic-size disorder is described analogously using the atomic-size-difference parameter commonly applied to high-entropy alloys [21]. For the 12-fold coordinated A site,

$$r_{\mathrm{avg}} = \sum_i x_i r_i, \qquad \delta_{\mathrm{size}} = \left[\sum_i x_i \left(1 - \frac{r_i}{r_{\mathrm{avg}}} \right)^2 \right]^{1/2}. \tag{2}$$

Here r_i is the Shannon ionic radius [22, 23]: 1.44 Å for Sr^{2+}, 1.61 Å for Ba^{2+}, 1.34 Å for Ca^{2+}, 1.49 Å for Pb^{2+} and 1.36 Å for La^{3+}. Pb-containing compositions have large δ_{mass} because of the large atomic mass of Pb. At the same 20% substitution level, Ca produces a larger δ_{size} than Pb, while Ba/Ca mixing increases δ_{size} further because Ba and Ca have the largest ionic-radius contrast among the A-site species considered. Comparison with the RDFs in Fig. 2b shows that these composition-based descriptors capture only part of the structural response. The large δ_{mass} of the Pb-containing system does not produce the strongest RDF broadening, whereas the broader features of the Ca-containing system are consistent with its larger size mismatch. Mass and size descriptors thus distinguish the nominal sources of A-site disorder, but they do not quantify how structural relaxation redistributes that disorder through the TiO_6 network.

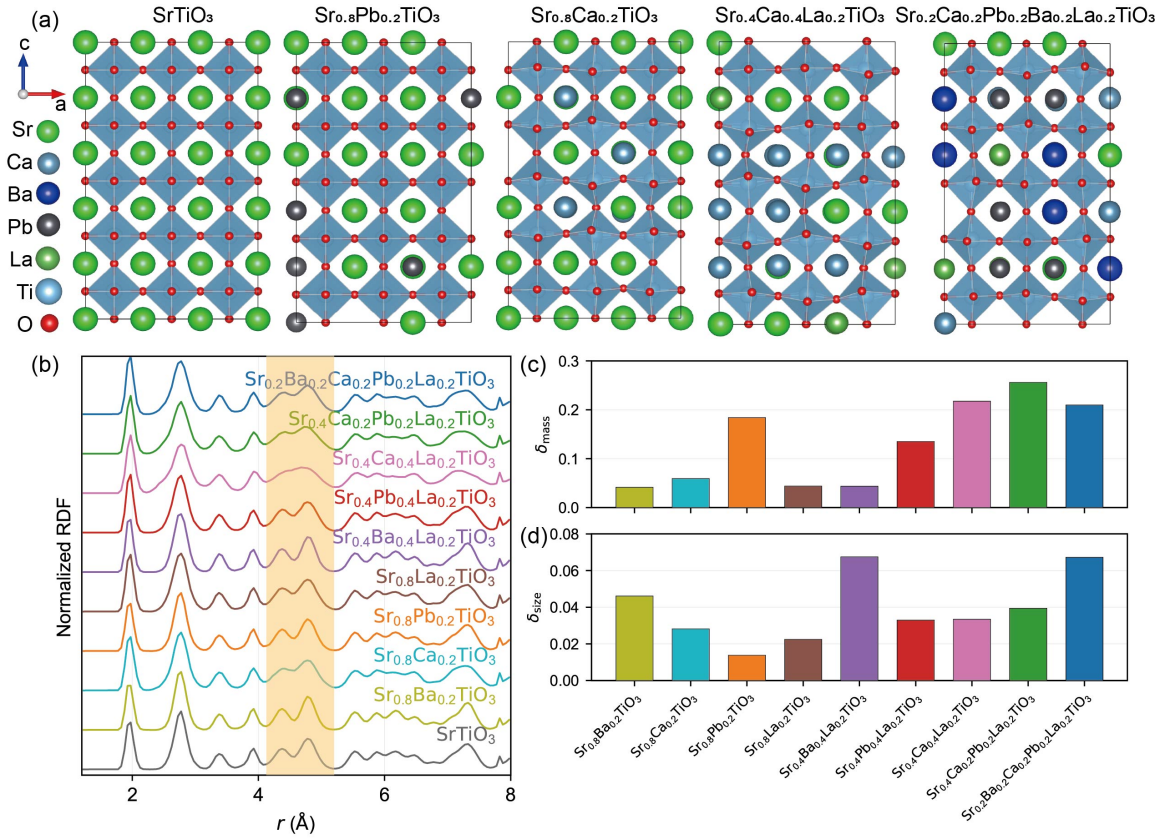


Figure 2: A-site disorder in $SrTiO_3$-based compositions. (a) Representative structures of $SrTiO_3$, $Sr_{0.8}Pb_{0.2}TiO_3$, $Sr_{0.8}Ca_{0.2}TiO_3$, $Sr_{0.4}Ca_{0.4}La_{0.2}TiO_3$ and $Sr_{0.2}Ba_{0.2}Ca_{0.2}Pb_{0.2}La_{0.2}TiO_3$. (b) Total radial distribution functions of selected compositions. (c-d) A-site mass fluctuation and ionic-size mismatch descriptors for the studied compositions.

The incomplete correspondence between the composition-based descriptors and RDF broadening indicates that nominal A-site disorder alone does not describe the response of the relaxed lattice. We therefore examine two complementary manifestations of this disorder in Fig. 3: the vibrational

density of states (DOS) obtained from the velocity autocorrelation function and the distribution of instantaneous per-atom virial-derived von Mises stresses pooled over the sampled 300 K MD trajectories. The DOS in Fig. 3a reveals distinct composition-dependent responses. Pb substitution introduces a pronounced low-frequency soft-mode feature. This behavior is consistent with Pb-based thermoelectrics such as PbTe, in which strongly anharmonic soft transverse-optical modes couple to heat-carrying acoustic phonons [24, 25]. Ca substitution, by contrast, produces broadening across the spectrum rather than a single dominant soft feature. This broadening is most evident in $Sr_{0.4}Ca_{0.4}La_{0.2}TiO_3$ and is consistent with the RDF evidence that Ca-driven size mismatch perturbs medium-range Ti-O and A-O correlations. Compositions approaching the high-entropy limit, particularly those containing both Pb and Ca, exhibit both signatures: a Pb-associated low-frequency contribution and broad spectral features associated with size-mismatch disorder. The DOS therefore provides a dynamical counterpart to the RDF trends, distinguishing the response associated with heavy Pb substitution from the broader lattice distortion induced by Ca. To determine how these vibrational signatures relate to the finite-temperature local stress landscape, we next examine the all-atom stress distributions in Fig. 3b.

For each sampled MD frame, the atom-resolved virial tensor $\mathbf{W}_i(t)$ associated with atom i was converted into a stress-like tensor using an average atomic volume,

$$\boldsymbol{\sigma}_i(t) = \frac{\mathbf{W}_i(t)}{V_{\mathrm{cell}}/N_{\mathrm{atom}}} \times 160.21, \tag{3}$$

where the numerical factor converts eV Å^{-3} to GPa. The instantaneous von Mises magnitude was then evaluated separately for every atom in every sampled frame,

$$\begin{aligned} s_i(t) = \Bigg\{ \frac{1}{2} \Big(& [\sigma_{xx,i}(t) - \sigma_{yy,i}(t)]^2 + [\sigma_{yy,i}(t) - \sigma_{zz,i}(t)]^2 \\ & + [\sigma_{zz,i}(t) - \sigma_{xx,i}(t)]^2 \\ & + 6[\sigma_{xy,i}^2(t) + \sigma_{yz,i}^2(t) + \sigma_{zx,i}^2(t)] \Big) \Bigg\}^{1/2}. \end{aligned} \tag{4}$$

For each representative structure, the instantaneous $s_i(t)$ values were pooled over all atoms and sampled frames to construct a normalized distribution. The normalized distributions were subsequently averaged over the representative disordered structures for each composition. We use $s_i(t)$ as an empirical descriptor of the instantaneous local stress environment, not as a true stress acting on an isolated atom or as a macroscopic residual stress. Increasing A-site disorder diversifies the local chemical environments and distorts the TiO_6 framework. The resulting broadening of the von Mises stress distributions in Fig. 3b reflects greater heterogeneity in the finite-temperature local stress landscape. We next compare this stress response with thermal transport.

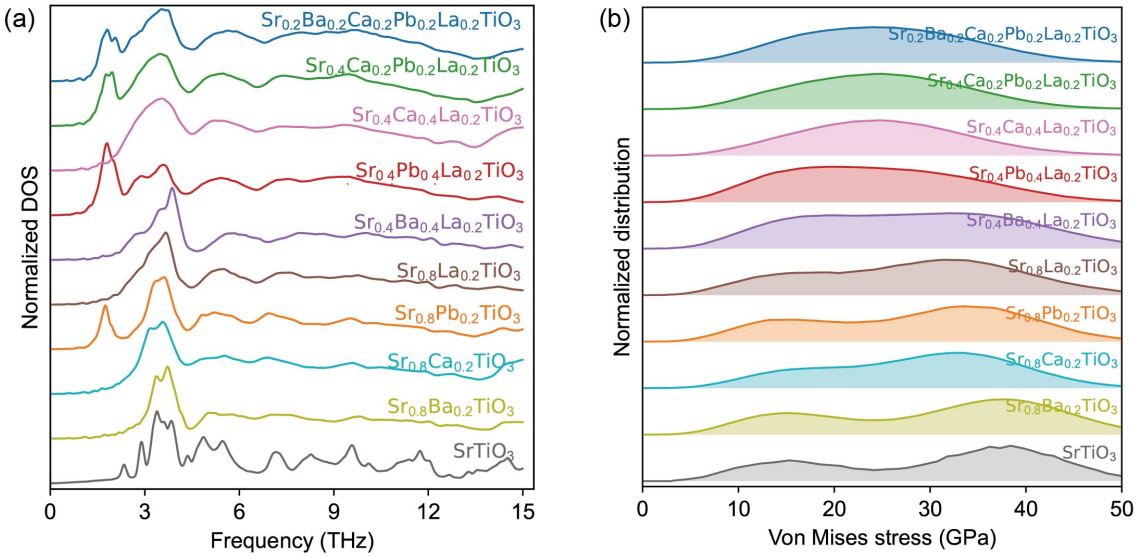


Figure 3: Vibrational density of states and von Mises stress distributions. (a) Vibrational density of states obtained from the velocity autocorrelation function. (b) Normalized instantaneous per-atom von Mises stress distributions at 300 K.

Figure 4a compares the lattice thermal conductivities of crystalline STO and the A-site-substituted systems. The distilled NEP gives a value of 8.93 W m^{-1} K^{-1} for crystalline STO, consistent with the reported range of 8–9 W m^{-1} K^{-1} [19]. This value provides a reference for the substituted compositions. Ba substitution causes only a small reduction in thermal conductivity. La substitution introduces a more complex local chemical environment, including changes in Ti valence, and produces a much larger decrease, consistent with its greater atomic mass relative to Sr. The contrast between the divalent Pb and Ca substitutions is particularly informative. Pb introduces a larger mass fluctuation and a pronounced soft-mode feature in the DOS, yet $Sr_{0.8}Ca_{0.2}TiO_3$ has a lower thermal conductivity than $Sr_{0.8}Pb_{0.2}TiO_3$. This result indicates that Ca-induced size mismatch and lattice distortion suppress heat transport more effectively than Pb-induced mass disorder. Across the broader entropy series, the thermal conductivity initially decreases rapidly as A-site configurational entropy increases. The decrease becomes much smaller once the thermal conductivity approaches 3 W m^{-1} K^{-1}. This behavior is evident across the three-, four- and five-component compositions, whose thermal conductivities change only modestly despite the increase in configurational entropy. From the four-component to the five-component composition, S_{conf} increases from $1.332R$ to $1.609R$, whereas the thermal conductivity decreases only from 2.95 to 2.77 W m^{-1} K^{-1}. The latter value remains above the Cahill-Pohl minimum of approximately 1.84 W m^{-1} K^{-1}. Thus, high-entropy A-site disorder strongly scatters phonons but does not eliminate all crystalline heat-carrying channels in the STO framework. Further reductions may be possible by optimizing the relative Ca and Pb contents or other compositional variables, but determining the absolute minimum thermal conductivity is beyond the scope of this work.

To determine which descriptor best tracks this reduction, Fig. 4b–e compares thermal conductivity with several structural and mechanical descriptors. The Pearson coefficient r is calculated across the compositions from each descriptor and its corresponding thermal conductivity. The mass-fluctuation descriptor in Fig. 4b has a moderate negative correlation with thermal conductivity ($r = -0.71$). Although the Pb-containing compositions have large δ_{mass}, they do not follow the same conductivity trend as the Pb-free systems. The size-mismatch descriptor in Fig. 4c shows a weaker correlation ($r = -0.53$), with the Ba- and La-containing systems deviating from the Ca-rich trend. Because these composition-based descriptors do not fully capture the conductivity trend,

we next examine distortion of the TiO_6 framework. Figure 4d quantifies this distortion using the dimensionless root-mean-square (RMS) variation in the Ti-O bond lengths,

$$D_{\mathrm{Ti-O}} = \left[\frac{1}{6} \sum_{i=1}^{6} \left(\frac{d_i - \bar{d}}{\bar{d}} \right)^2 \right]^{1/2}, \tag{5}$$

where d_i denotes each of the six nearest-neighbor Ti-O bond lengths and $\bar{d}$ is their mean. Figure 4d reports the average $D_{\mathrm{Ti-O}}$ over all Ti sites in the relaxed supercell, with horizontal error bars showing the standard deviation across the sites. The correlation with thermal conductivity ($r = -0.83$) is stronger than those obtained for δ_{mass} and δ_{size}. This result indicates that the conductivity reduction is more closely associated with local TiO_6 distortion than with A-site compositional disorder alone.

More fundamentally, multi-element A-site substitution and TiO_6 distortion redistribute the finite-temperature local stress landscape. In Fig. 4e, this redistribution is quantified by the shift of the dominant peak in the A-site von Mises stress distribution relative to ordered $SrTiO_3$. Among the descriptors compared in Fig. 4b–e, the A-site stress peak shift gives the strongest correlation with thermal conductivity ($r = -0.84$), as indicated by the dashed guide line in Fig. 4e. Consistent with this result, the site-resolved analysis in Fig. S5 shows that the O-site stress peak shift also correlates strongly with thermal conductivity ($r = 0.91$), whereas the Ti-site shift is essentially uncorrelated ($r = -0.01$). This contrast is consistent with the stress response to complex A-site chemical environments being transmitted through the oxygen sublattice of the TiO_6 framework. Taken together, these trends suggest that the conductivity reduction is more directly associated with redistribution of the finite-temperature local stress landscape than with A-site mass or size descriptors alone. We next examine how this stress-related disorder is reflected in the phonon spectra.

To identify a phonon-spectral counterpart to the stress-related transport trend in Fig. 4, we calculate the dynamical structure factor $S(\mathbf{Q}, E)$. Relative to $SrTiO_3$ (Fig. 5a), Ba substitution causes only minor changes in the spectrum (Fig. 5b), consistent with its weak effect on thermal conductivity. Pb substitution adds low-frequency spectral weight along the dashed guide in Fig. 5c, producing a soft-mode-like response. Ca substitution has a different effect. In $Sr_{0.8}Ca_{0.2}TiO_3$, the spectral intensity near 4 THz along the Γ–X direction becomes more diffuse (Fig. 5d), indicating stronger phonon broadening. When Pb and Ca coexist in the multicomponent systems, both signatures are present. The four- and five-component compositions in Fig. 5e,f show enhanced low-frequency weight together with broad, diffuse intensity near 4 THz. These results associate Pb primarily with the soft-mode-like low-frequency response and Ca with spectral broadening. Their coexistence in the high-entropy compositions is characteristic of enhanced anharmonicity.

Figure 6 connects these spectral changes to local anharmonic dynamics and phonon transport parameters. In Fig. 6a, the relative finite-temperature free-energy profile for Ti off-centering is reconstructed from the probability distribution $P(|u_{\mathrm{Ti}}|)$ using $\Delta F(|u_{\mathrm{Ti}}|) = -k_{\mathrm{B}}T \ln P(|u_{\mathrm{Ti}}|)$, with the minimum set to zero [26]. Compared with $SrTiO_3$ and Ba-doped STO, the Pb- and Ca-containing systems have lower free-energy penalties at large Ti off-centering amplitudes, indicating softer and more anharmonic local potentials. The reduction is more obviously in the multicomponent A-site systems, suggesting that a wider range of Ti off-centering amplitudes becomes thermally accessible as chemical complexity increases. Figure 6b provides a closer comparison through line cuts of $S(\mathbf{Q}, E)$ at $Q = (2.1, 0, 0)$. Pb substitution splits the low-frequency feature associated with the soft-mode-like response, whereas Ca substitution mainly broadens the peak. When Pb and Ca coexist, the low-frequency peak remains pronounced, while the split feature is broader than in the Pb-only system.

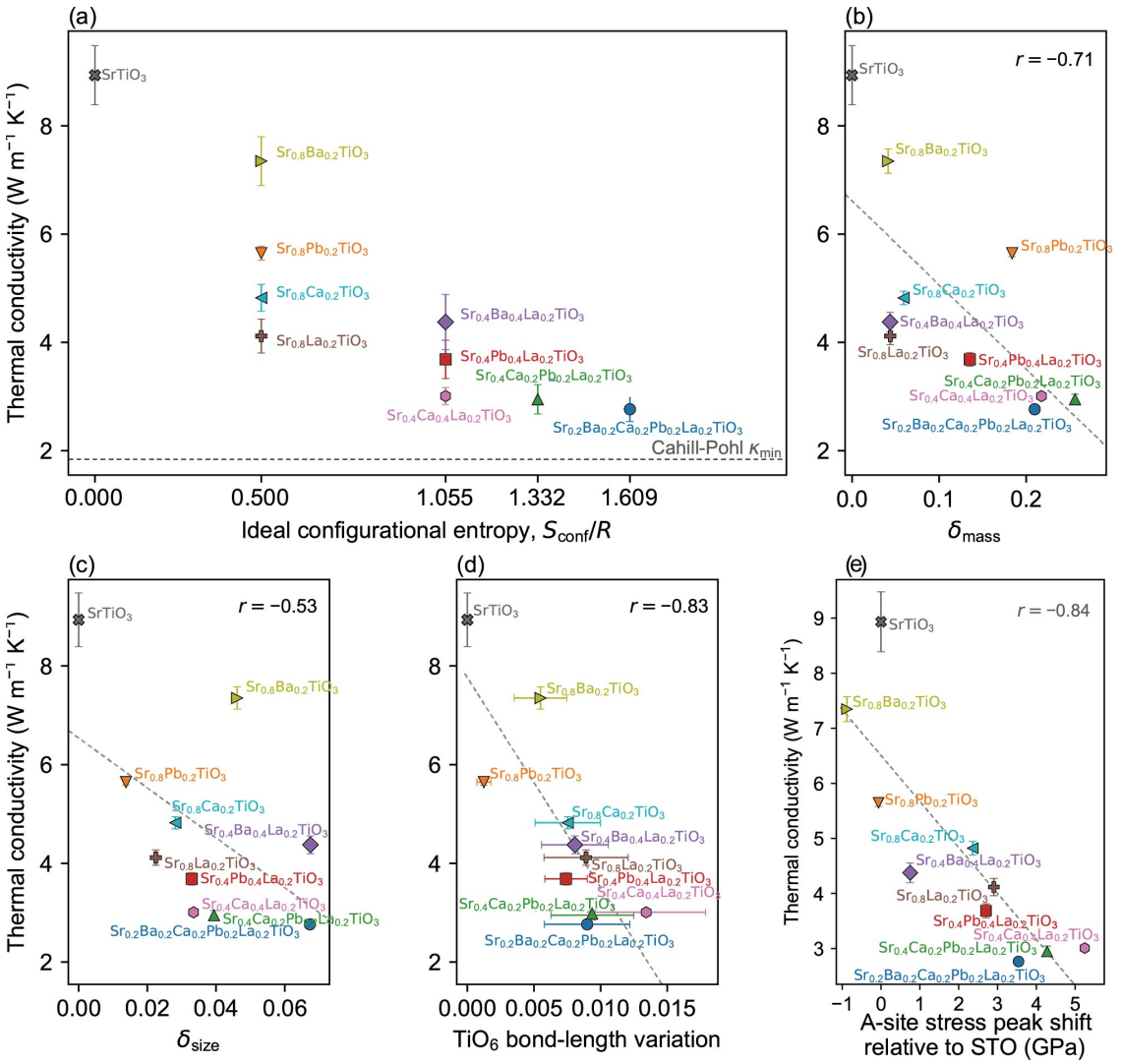


Figure 4: Descriptor dependence of lattice thermal conductivity. (a) Thermal conductivity as a function of ideal configurational entropy; the horizontal dashed line marks the Cahill-Pohl minimum thermal conductivity. (b) Thermal conductivity versus A-site mass fluctuation. (c) Thermal conductivity versus A-site ionic-size mismatch. (d) Thermal conductivity versus the RMS TiO_6 bond-length distortion, averaged over all Ti sites in the relaxed supercell. (e) Thermal conductivity versus the shift of the dominant peak in the composition-averaged, time-pooled instantaneous A-site $s_i(t)$ distribution relative to ordered $SrTiO_3$. Pearson coefficients r are calculated from the plotted central values, and grey dashed lines in (b)–(e) are linear guides to the eye.

To assess how A-site substitution alters acoustic heat transport, we examine the group velocity and effective spectral broadening of the longitudinal acoustic branch. In the phonon-gas picture, $\kappa = \frac{1}{3}Cv_g^2\tau$, where C is the heat capacity, v_g is the phonon group velocity and τ is the phonon lifetime. A shorter lifetime generally produces a broader spectral feature. We estimate v_g from the slope of the fitted longitudinal acoustic mode by tracking its peak frequency as a function of reciprocal-space distance (Fig. 6b). The resulting value for STO is 7926 m s^{-1}, close to the reported longitudinal acoustic velocity of 7700 m s^{-1} [27]. Figure 6c shows a strong negative correlation between v_g and δ_{mass} ($r = -0.99$). The correlation with the A-site stress peak shift is weaker ($r = -0.59$; Fig. 6d). The Pb-containing system shows a large velocity reduction despite its slightly negative peak shift, whereas the Ca-containing system has a positive peak shift but retains

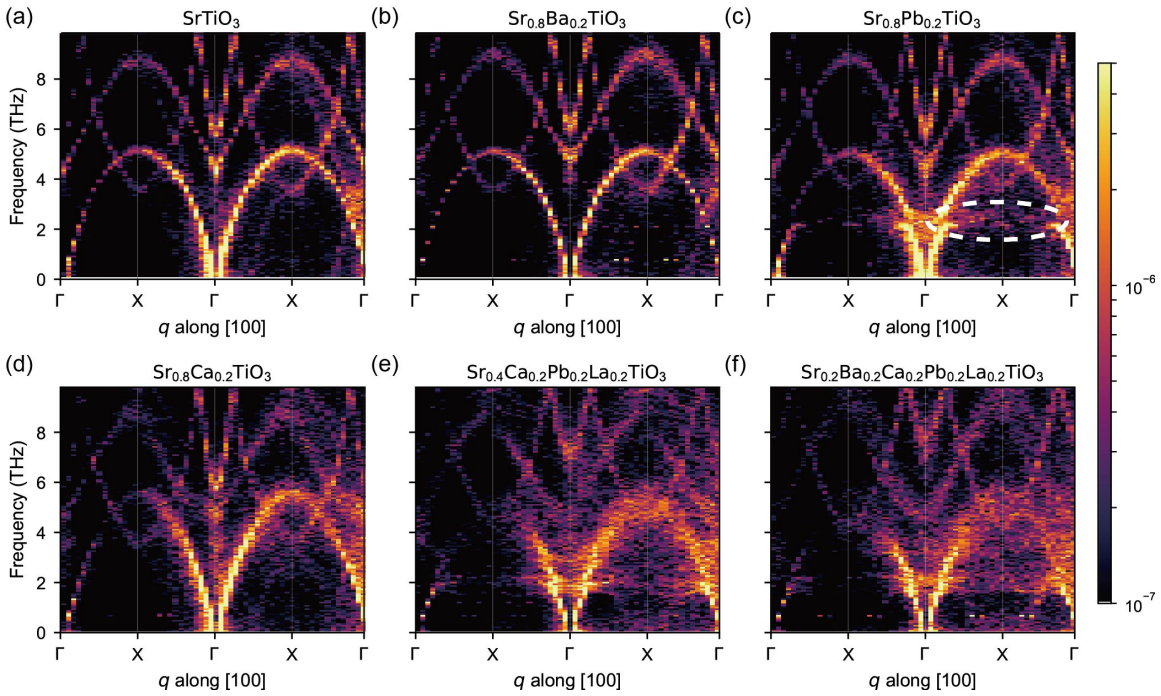


Figure 5: Dynamical structure factors $S(\mathbf{Q}, E)$ of representative STO-based compositions along the Γ–X direction. (a) $SrTiO_3$, (b) $Sr_{0.8}Ba_{0.2}TiO_3$, (c) $Sr_{0.8}Pb_{0.2}TiO_3$, (d) $Sr_{0.8}Ca_{0.2}TiO_3$, (e) $Sr_{0.4}Ca_{0.2}Pb_{0.2}La_{0.2}TiO_3$ and (f) $Sr_{0.2}Ba_{0.2}Ca_{0.2}Pb_{0.2}La_{0.2}TiO_3$.

a higher velocity. Mass fluctuation therefore tracks the reduction in sound velocity, but it does not explain why Ca suppresses thermal conductivity more strongly than Pb.

We then evaluate a lifetime-like spectral-broadening descriptor from the same $S(\mathbf{Q}, E)$ fits without assigning a complete mode-resolved Boltzmann lifetime. This conservative treatment is needed because increasing A-site complexity strongly reshapes the spectra: some phonon modes broaden, split or merge into a diffuse background, so a direct comparison of conventional phonon linewidths would depend sensitively on how individual peaks are assigned. For each constant-Q cut along $Q = (2+q, 0, 0)$, R_{peak} is defined as the integrated area of the fitted coherent peak-like phonon components, whereas R_{bg} is the integrated area of the fitted diffuse background over the same energy window, as shown in Fig. S6. The ratio $\bar{R}_{\mathrm{peak}}/\bar{R}_{\mathrm{bg}}$ is then averaged over the analyzed Q range. A smaller ratio indicates that spectral weight is transferred from sharp propagating features into a diffuse background, corresponding to stronger effective broadening and shorter lifetime-like spectral coherence. This comparison separates two points. First, $Sr_{0.8}Ca_{0.2}TiO_3$ has a smaller $\bar{R}_{\mathrm{peak}}/\bar{R}_{\mathrm{bg}}$ than $Sr_{0.8}Pb_{0.2}TiO_3$, even though Ca produces a smaller mass fluctuation than Pb (Fig. 6e). This indicates that the lower thermal conductivity of Ca-doped STO is associated with stronger phonon scattering and shorter lifetime-like spectral coherence. Second, the descriptor correlation also favors the stress picture: $\bar{R}_{\mathrm{peak}}/\bar{R}_{\mathrm{bg}}$ has only a weak relation with δ_{mass} ($r = -0.26$), but correlates much more clearly with the A-site stress peak shift ($r = -0.87$, Fig. 6f). Thus, while mass fluctuation is closely associated with the reduction of group velocity, the peak-to-background analysis shows that stress redistribution better captures the loss of sharp propagating phonon features. The A-site stress peak shift therefore links A-site chemical complexity to stronger effective spectral broadening, pointing to phonon lifetime suppression as an important microscopic contribution to the low thermal conductivity in high-entropy STO.

La substitution is commonly used in STO-based thermoelectrics to reduce lattice thermal conductivity while improving electronic transport [2]. Because La substitution can also alter the

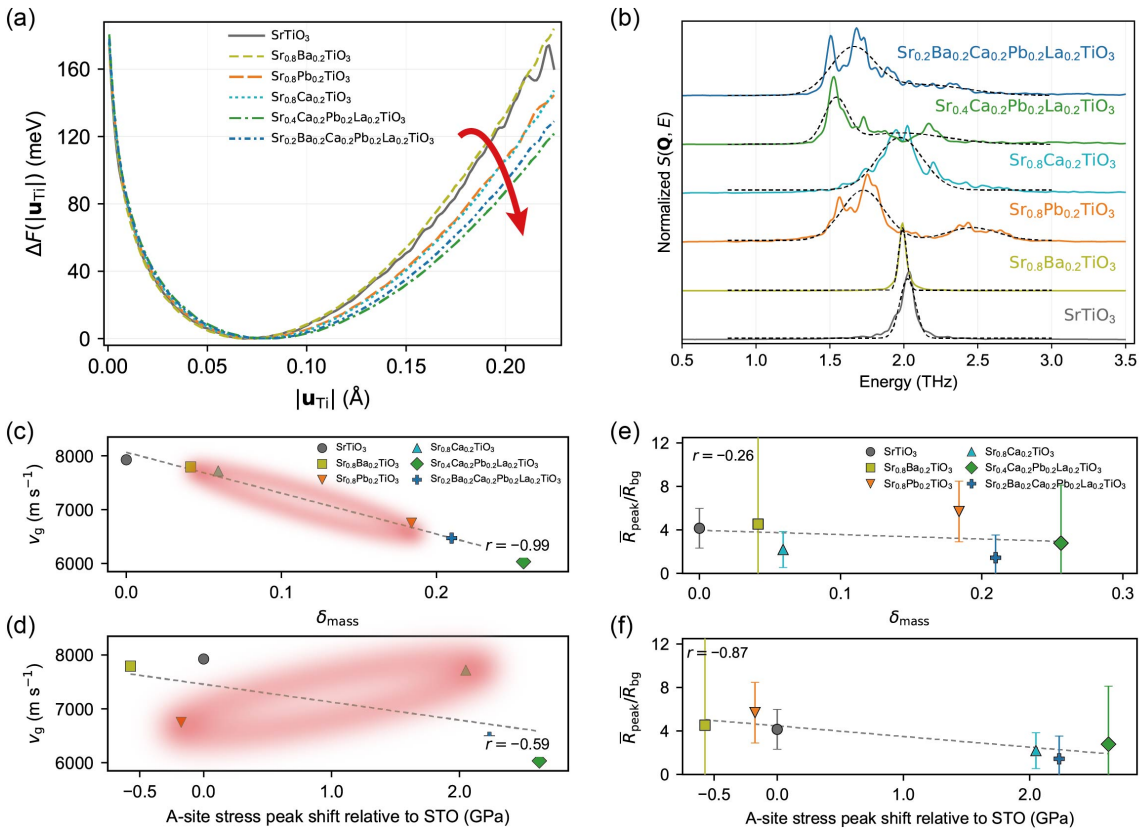


Figure 6: Anharmonic local dynamics and effective longitudinal-acoustic spectral broadening. (a) Free-energy profile $\Delta F(|u_{\mathrm{Ti}}|) = -k_{\mathrm{B}}T \ln P(|u_{\mathrm{Ti}}|)$ reconstructed from the local Ti off-centering amplitude. (b) Normalized $S(\mathbf{Q}, E)$ line cuts at $Q = (2.1, 0, 0)$ for the longitudinal acoustic branch, showing Pb-induced peak splitting and Ca-induced peak broadening. (c,d) Group velocity v_g of the longitudinal acoustic branch plotted against A-site mass fluctuation and the A-site stress peak shift relative to STO. (e,f) Ratio between the fitted peak area and diffuse background area, $\bar{R}_{\mathrm{peak}}/\bar{R}_{\mathrm{bg}}$, averaged over the sampled wave vectors from $Q = (2.1, 0, 0)$ to $Q = (2.5, 0, 0)$ and plotted against A-site mass fluctuation and the A-site stress peak shift relative to STO. Pearson coefficients r are calculated from the plotted central values, and grey dashed lines are linear guides to the eye.

Ti-site valence, we examined whether the descriptor hierarchy identified above is specific to the La-containing chemical space. We repeated the thermal-transport and descriptor analysis for an analogous Cd-containing composition series comprising A-site mixtures of Sr, Pb, Ba, Ca and Cd (Fig. S7). The correlations of thermal conductivity with A-site mass fluctuation and ionic-size mismatch remain relatively weak ($r = -0.55$ and -0.66, respectively), whereas TiO_6 bond-length distortion and the A-site stress peak shift show substantially stronger correlations ($r = -0.90$ and -0.91). The Cd-containing series, which does not involve the La-associated Ti-site valence change, therefore reproduces the descriptor hierarchy found for the La-containing systems. This result supports the conclusion that local structural distortion and stress redistribution describe the reduction in thermal conductivity more consistently than composition-only mass and size descriptors.

Overall, this work establishes two complementary results for A-site-disordered STO. First, the fine-tuned MACE-guided NEP distillation workflow provides an effective route to interatomic potentials for chemically complex high-entropy oxides that are difficult to fit directly, as demonstrated here for the La-containing composition space. Fine-tuning produces an accurate teacher model, while distillation transfers this description to a compact potential suitable for large-scale thermal-transport and phonon-dynamics simulations. Second, the reduction in lattice thermal con-

ductivity cannot be described by configurational entropy or mass fluctuation alone. Increasing A-site complexity rapidly lowers the thermal conductivity, but the decrease becomes much smaller once the system enters the low-conductivity regime. TiO_6 distortion and the A-site stress peak shift describe the conductivity trend more consistently than the A-site mass and size descriptors. In these doping elements, Pb primarily introduces a low-frequency soft-mode-like response, whereas Ca produces stronger spectral broadening and greater heterogeneity in the finite-temperature local stress landscape. Local stress disorder connects A-site chemical complexity, anharmonic phonon spectra and suppressed heat transport in STO-based perovskites. Taken together, the fine-tuning and distillation strategy and the stress-based transport analysis provide a transferable framework for investigating other high-entropy oxide thermoelectrics.

Methods

Model construction and compositions

All models were built from the cubic perovskite $SrTiO_3$ framework by substituting only the A-site sublattice, while keeping the TiO_3 framework stoichiometric. The basic configurational cell contains 30 ABO_3 formula units, corresponding to 150 atoms. This cell size allows the 20% A-site fraction used throughout the work to be represented by six A-site atoms.The studied compositions include pristine $SrTiO_3$ and the single-substitution systems $Sr_{0.8}Ba_{0.2}TiO_3$, $Sr_{0.8}Ca_{0.2}TiO_3$, $Sr_{0.8}Pb_{0.2}TiO_3$ and $Sr_{0.8}La_{0.2}TiO_3$. We also considered the three-component systems $Sr_{0.4}Ba_{0.4}La_{0.2}TiO_3$, $Sr_{0.4}Ca_{0.4}La_{0.2}TiO_3$ and $Sr_{0.4}Pb_{0.4}La_{0.2}TiO_3$, together with the four-component $Sr_{0.4}Ca_{0.2}Pb_{0.2}La_{0.2}TiO_3$ and the five-component high-entropy $Sr_{0.2}Ba_{0.2}Ca_{0.2}Pb_{0.2}La_{0.2}$-$TiO_3$. For each composition, the required number of Sr, Ba, Ca, Pb and La atoms was assigned to the A-site sublattice according to the nominal molar fractions.

For the disordered compositions, multiple A-site arrangements were generated to sample configurational disorder. Binary single-dopant systems were represented by independent SQS-like configurations generated using ICET [28]. For selected multi-component compositions, different A-site short-range-order (SRO) states were then generated from fixed-composition configurations using a Short-range Ordering based Swapping method [29]. In this procedure, A-site species are swapped while preserving the overall composition, allowing representative second-neighbor A-site pair correlations, such as Ba–Ba, Ca–Ca or Pb–Pb pairs, to be varied systematically. All 150-atom configurational cells were structurally relaxed before being used as parent cells for larger MD models. The production MD simulations used 4×4×4 replications of these parent cells, giving 9600-atom supercells for thermal-transport and local-stress analyses. To assess whether the conclusions depend on a particular A-site arrangement, we compared thermal conductivities across the SRO-sampled structures. The SRO-induced spread in thermal conductivity is small compared with the composition-driven changes discussed in the main text, so composition-averaged values are used for the descriptor analysis. The SRO comparison is shown in Fig. S4.

DFT calculations and MACE fine-tuning

The DFT reference data used for MACE fine-tuning were obtained from single-point VASP calculations on preselected STO-based disordered configurations. Candidate structures were first generated by adjusting A-site short-range order through atom-swapping transformations to obtain the corresponding initial configurations. These structures were then supplemented with configurations sampled from 500 and 1000 K trajectories to enrich the local chemical and strain environments relevant to high-entropy A-site disorder. VASP outputs were parsed from the corresponding OUT-

CAR files and converted into a training database containing structures, total energies, atomic forces. All DFT calculations used the PBE exchange-correlation functional in VASP 6.5.1 with an energy cutoff of 550 eV. The VASP PAW datasets Sr_sv, Ba_sv, Ca_pv, La, Pb, Ti and O were used for the corresponding elements. Electronic convergence was controlled with EDIFF = 1e-5. Brillouin-zone sampling used KSPACING = 0.25 with gamma-centered meshes.

The MACE teacher model was obtained by fine-tuning a pretrained MACE-MP-0 medium model on the DFT-labelled STO dataset. The merged DFT pool contained 615 structures. The final dataset was split into 492 training, 61 validation and 62 test structures. Fine-tuning used a weighted energy-force loss with energy and force weights of 1.0 and 3.0, respectively. The radial cutoff was set as 6 Å. The batch size of is set as 16 and the learning rate is set as 5×10^{-5}. Model quality was evaluated by comparing the pretrained and fine-tuned MACE predictions against DFT on both training and test splits as shown in Fig. S1. The fine-tuned MACE model was then compiled and used as the teacher model for the NEP distillation step. Besides, a Cd-containing dataset was constructed by replacing La with Cd while retaining the same number of DFT-labelled structures as in the La-containing dataset. Direct NEP models for the La- and Cd-containing spaces were trained and evaluated using a consistent workflow, and their parity plots are compared in Fig. S2. This comparison was used to assess the direct learnability of the two chemical spaces.

MACE-guided NEP distillation and molecular dynamics

To transfer the accuracy of the fine-tuned MACE teacher to a more efficient potential for large-scale MD, we distilled the teacher model into a neuroevolution potential (NEP). A representative set containing 2417 structures was selected from the available STO-based configuration space using Dimensionality-Reduced Encoded Clusters with sTratified (DIRECT) sampling [30]. These structures were labelled by the compiled fine-tuned MACE teacher, producing MACE-reference energies and forces for NEP training. The 2417 labelled structures were split into 2175 training and 242 test configurations. The NEP training loss included energy and force terms with weights $\lambda_E = 1.0$ and $\lambda_F = 3.0$. The radial cutoff was set as 6 Å and the angular cutoff was set as 4 Å. The final NEP model used here corresponds to the last recorded training step at 4600. The distilled NEP was then used for all subsequent structural relaxation, thermal transport and phonon dynamics simulations because it allows substantially larger simulation cells and longer trajectories than direct MACE-driven MD.

To quantify the computational benefit of distillation, we benchmarked the fine-tuned MACE teacher and distilled NEP on the same NVIDIA A100-SXM4-80GB GPU (Fig. S3). Systems containing 150 to 9600 atoms were constructed from the reduced composition $BaCaLaPbSrTi_5O_{15}$. Both models were run for 50 simulation steps at each system size. MACE used the CUDA-enabled ASE `MACECalculator` without cuEquivariance, whereas NEP used native GPUMD. NEP was faster across the full size range, with speedups of 52.2-fold at 150 atoms and 555-fold at 9600 atoms. At 9600 atoms, MACE required 70.83 GB of GPU memory, approximately 48.4 times the NEP requirement. These results show that the distilled NEP provides the speed and memory efficiency needed for large-scale, long-timescale MD simulations.

Phonon analyses and thermal conductivity calculation

Phonon-related quantities were evaluated from the same NEP-based finite-temperature MD framework. The vibrational density of states was obtained from the Fourier transform of the

velocity autocorrelation function [31, 32],

$$g(\omega) = \int_{-\infty}^{\infty} \frac{\langle \sum_i \mathbf{v}_i(t) \cdot \mathbf{v}_i(0) \rangle}{\langle \sum_i \mathbf{v}_i(0) \cdot \mathbf{v}_i(0) \rangle} e^{i\omega t}\, dt, \tag{6}$$

where $\mathbf{v}_i(t)$ is the velocity of atom i and the brackets denote an equilibrium time average. The dynamical structure factor was calculated from the time correlation function [33–35],

$$S(\mathbf{Q}, \omega) = \frac{1}{2\pi N} \int_{-\infty}^{\infty} \langle \rho_{\mathbf{Q}}(t) \rho_{-\mathbf{Q}}(0) \rangle\, e^{i\omega t}\, dt, \qquad \rho_{\mathbf{Q}}(t) = \sum_j e^{-i\mathbf{Q}\cdot\mathbf{r}_j(t)}, \tag{7}$$

with $E = \hbar\omega$. The calculated $S(\mathbf{Q}, E)$ spectra along the selected reciprocal-space path were used to compare spectral softening and broadening among representative compositions. For the linewidth analysis, selected constant-Q cuts were fitted to extract peak positions and full widths at half maximum, and the group velocity was estimated from the slope of the low-frequency peak dispersion. These quantities were used only as relative descriptors across compositions, while the thermal conductivity trends were taken from the equilibrium MD heat-current analysis described above.

Thermal conductivities were calculated from equilibrium molecular dynamics (EMD) simulations using the heat-current autocorrelation workflow implemented in GPUMD. For each structure, the simulation cell was first replicated into a supercell, and initial velocities were assigned using different random seeds. The systems were then equilibrated at 300 K under an NVT thermostat and subsequently continued into NVE production trajectories without further modification. For each representative structure, 20 independent runs were performed. The simulations used a time step of 1 fs, with an NVT equilibration stage of 100000 steps and an NVE production stage of 100000 steps. The thermostat time constant was set to 100 fs, and the heat current was sampled every 10 steps. The heat-current autocorrelation function was accumulated with 10000 correlation points and an output interval of 10. The directional conductivities κ_{xx}, κ_{yy} and κ_{zz} were obtained from the running Green–Kubo integral, and the isotropic lattice thermal conductivity was calculated as $\kappa_{\mathrm{iso}} = (\kappa_{xx} + \kappa_{yy} + \kappa_{zz})/3$. For each run, the reported conductivity was extracted by fitting the latter half of the running conductivity curve, and the final values were averaged over independent runs.

Acknowledgements

This work acknowledged the support from Zhongguancun Academy (XTS0063), National Natural Science Foundation of China (No. 12304040), GuangDong Basic and Applied Basic Research Foundation (Grant No. 2023A1515110762), and Key Laboratory of Green Extraction & Efficient Utilization of Light Rare-Earth Resources (Inner Mongolia University of Science and Technology) of Ministry of Education (No. REKF26003). Bonan Zhu is supported by the Nature Science Foundation of China (Grant No. 12404068). This work was supported by the Fundamental Research Funds for the Central Universities (Beijing Institute of Technology 284 academic starting grant RCPT-6120230091).

Contributions

Y. L. performed the simulations, analyzed the data, and contributed to the writing of the manuscript. M. L., H. D., B. W., and Y. L. contributed to the analysis of the data used in this work. B. W., B. Z., and Z. L. conceived the project and contributed to the analysis and writing of the manuscript. All authors reviewed the manuscript.

Data Availability

All data and methodological details required to reproduce the calculations are provided in the main text, Methods, and Supplementary Information.

Competing interests

The authors declare no competing interests.

References

[1] Zheng, Y. *et al.* Electrical and thermal transport behaviours of high-entropy perovskite thermoelectric oxides. *Journal of Advanced Ceramics* **10**, 377–384 (2021).

[2] Zheng, Y. *et al.* Carrier-phonon decoupling in perovskite thermoelectrics via entropy engineering. *Nature Communications* **15**, 7650 (2024).

[3] Liu, S. *et al.* High-entropy thermoelectric materials: Advances, challenges, and future opportunities. *ACS Energy Letters* **10**, 925–934 (2025).

[4] Jiang, B. *et al.* High-entropy-stabilized chalcogenides with high thermoelectric performance. *Science* **371**, 830–834 (2021).

[5] Jiang, B. *et al.* High figure-of-merit and power generation in high-entropy gete-based thermoelectrics. *Science* **377**, 208–213 (2022).

[6] Luo, Y. *et al.* High thermoelectric performance in the new cubic semiconductor agsnsbse$_3$ by high-entropy engineering. *Journal of the American Chemical Society* **142**, 15187–15198 (2020).

[7] Ma, Z. *et al.* High entropy semiconductor agmngesbte$_4$ with desirable thermoelectric performance. *Advanced Functional Materials* **31** (2021).

[8] Zhang, X. *et al.* Ultralow lattice thermal conductivity and improved thermoelectric performance in a Hf-free half-Heusler compound modulated by entropy engineering. *Journal of Materials Chemistry A* **11**, 8150–8161 (2023).

[9] Ahmad, A. *et al.* Largely enhanced thermoelectric performance in p-type bi$_2$te$_3$-based materials through entropy engineering. *Energy & Environmental Science* **17**, 695–703 (2024).

[10] Braun, J. L. *et al.* Charge-induced disorder controls the thermal conductivity of entropy-stabilized oxides. *Advanced Materials* **30** (2018).

[11] Zhang, P. *et al.* High-entropy (ca0.2sr0.2ba0.2la0.2pb0.2)tio3 perovskite ceramics with a-site short-range disorder for thermoelectric applications. *Journal of Materials Science & Technology* **97**, 182–189 (2022).

[12] Roychowdhury, S., Biswas, R. K., Dutta, M., Pati, S. K. & Biswas, K. Phonon localization and entropy-driven point defects lead to ultralow thermal conductivity and enhanced thermoelectric performance in $(SnTe)_{1-2x}(SnSe)_x(SnS)_x$. *ACS Energy Letters* **4**, 1658–1662 (2019).

[13] Gao, H. *et al.* Adaptable sublattice stabilized high-entropy materials with superior thermoelectric performance. *Energy & Environmental Science* **16**, 6046–6057 (2023).

[14] Wang, W. *et al.* Tailoring local chemical fluctuation of high-entropy structures in thermoelectric materials. *Science Advances* **10** (2024).

[15] Wang, J. *et al.* Atomic to nanoscale chemical fluctuations: The catalyst for enhanced thermoelectric performance in high-entropy materials. *Science Advances* **11** (2025).

[16] Geng, X., Zhang, W., Wang, L.-W. & Meng, X. Origin of the machine learning forces field errors across metal elements. *npj Computational Materials* **12**, 102 (2026).

[17] Feng, T., Zhao, J., Liang, W. & Lu, G. Molecular dynamics simulations of lanthanum chloride by deep learning potential. *Computational Materials Science* **210**, 111014 (2022).

[18] Yan, Z., Tang, S. & Zhu, Y. A perspective on training machine learning force fields for solid-state electrolyte materials. *arXiv preprint arXiv:2603.07425* (2026).

[19] Wang, Q. *et al.* Phonon transport in freestanding ${\text{SrTiO}}_{3}$ down to the monolayer limit. *Physical Review B* **108**, 115435 (2023).

[20] Gurunathan, R. *et al.* Mapping thermoelectric transport in a multicomponent alloy space. *Advanced Electronic Materials* **8**, 2200327 (2022).

[21] Wang, Z., Qiu, W., Yang, Y. & Liu, C. T. Atomic-size and lattice-distortion effects in newly developed high-entropy alloys with multiple principal elements. *Intermetallics* **64**, 63–69 (2015).

[22] Shannon, R. D. Revised effective ionic radii and systematic studies of interatomic distances in halides and chalcogenides. *Acta Crystallographica Section A* **32**, 751–767 (1976).

[23] Jia, Y. Q. Crystal radii and effective ionic radii of the rare earth ions. *Journal of Solid State Chemistry* **95**, 184–187 (1991).

[24] Delaire, O. *et al.* Giant anharmonic phonon scattering in pbte. *Nature Materials* **10**, 614–619 (2011).

[25] Ju, S., Shiga, T., Feng, L. & Shiomi, J. Revisiting pbte to identify how thermal conductivity is really limited. *Physical Review B* **97** (2018).

[26] Frenkel, D. & Smit, B. *Understanding Molecular Simulation: From Algorithms to Applications* (Academic Press, San Diego, 2002), 2 edn.

[27] Shayduk, R. *et al.* Femtosecond x-ray diffraction study of multi-thz coherent phonons in srtio$_3$. *Applied Physics Letters* **120**, 202203 (2022).

[28] Ångqvist, M. *et al.* ICET – A Python Library for Constructing and Sampling Alloy Cluster Expansions. *Advanced Theory and Simulations* **2**, 1900015 (2019).

[29] Liao, J. *et al.* Modeling short-range order in high-entropy cation-disordered rocksalt-type cathodes. *Advanced Energy Materials* **15**, 2501857 (2025).

[30] Qi, J., Ko, T. W., Wood, B. C., Pham, T. A. & Ong, S. P. Robust training of machine learning interatomic potentials with dimensionality reduction and stratified sampling. *npj Computational Materials* **10**, 43 (2024).

[31] DICKEY, J. M. & PASKIN, A. Computer simulation of the lattice dynamics of solids. *Physical Review* **188**, 1407–1418 (1969).

[32] Weadock, N. J. *et al.* The nature of dynamic local order in $CH_3NH_3PbI_3$ and $CH_3NH_3PbBr_3$. *Joule* **7**, 1051–1066 (2023).

[33] Van Hove, L. Correlations in space and time and born approximation scattering in systems of interacting particles. *Physical Review* **95**, 249–262 (1954).

[34] Vineyard, G. H. Scattering of slow neutrons by a liquid. *Physical Review* **110**, 999–1010 (1958).

[35] Lovesey, S. W. *Theory of Neutron Scattering from Condensed Matter* (Clarendon Press, Oxford, 1984).

Supplementary Files

This is a list of supplementary files associated with this preprint. Click to download.

- SI.pdf